Condensed Layer Deposition of Nanoscopic TiO_2 Overlayers on High Surface Area Electrocatalysts

Daniela V. Fraga Alvarez[1,2,3], Zhexi Lin[1,2,3], Zixiao Shi[4], Amanda F. Baxter[1], Emily D. Wang[1], Dhruti Kuvar[1], Nafis Mahmud[6], Muftah H El-Naas[6], Héctor D. Abruña [4], David A. Muller[5], Daniel V. Esposito[1,2,3*],

Columbia University in the City of New York

[1]Department of Chemical Engineering

[2]Columbia Electrochemical Energy Center

[3]Lenfest Center for Sustainable Energy

500 W. 120th St., New York, NY 10027

Cornell University

[4]Department of Chemistry and Chemical Biology

[5]School of Applied and Engineering Physics

Ithaca, NY, USA

[6]Gas Processing Center

Qatar University

P.O. Box 2713, Al Tarfa Street

Doha, Qatar

Corresponding Author
*Daniel Esposito: de2300@columbia.edu

Abstract

Encapsulating an electrocatalytic material with a semi-permeable, nanoscopic oxide overlayer offers a promising approach to enhancing its stability, activity, and/or selectivity compared to an unencapsulated electrocatalyst. However, applying nanoscopic oxide encapsulation layers to high surface area electrodes, such as nanoparticle-supported porous electrodes is a challenging task. This study demonstrates that the recently developed condensed layer deposition (CLD) method can be used for depositing nanoscopic (sub-10 nm thick) titanium dioxide (TiO_2) overlayers onto high surface area platinized carbon foam electrodes. Characterization of the overlayers by transmission electron microscopy (TEM) and electron energy loss spectroscopy (EELS) showed that the films are amorphous, while X-ray photoelectron microscopy confirmed that they exhibit a TiO_2 stoichiometry. Electrodes were also characterized by hydrogen underpotential deposition (H_{upd}) and carbon monoxide (CO) stripping, demonstrating that the Pt electrocatalysts remain electrochemically active after encapsulation. Additionally, copper underpotential deposition (Cu_{upd}) measurements revealed that TiO_2 overlayers are effective at blocking Cu^{2+} from reaching the TiO_2/Pt buried interface and were used to estimate that between 43-98% of Pt surface sites were encapsulated. Overall, this study shows that CLD is a promising approach for depositing nanoscopic protective overlayers on high surface area electrodes.

Keywords: electrocatalysis, oxide overlayers, condensed layer deposition, buried interfaces, wet chemical synthesis, platinum, titanium oxide.

I. Introduction

Electrocatalytic processes offer many promising avenues to harness electricity generated by renewable sources to decarbonize the chemical industry.[1] However, improvements in the activity, selectivity, and stability of state-of-the-art electrocatalysts are necessary to make electrochemical processes more energy-efficient and economically competitive with today's fossil fuel-based chemical processes. Approaches for enhancing catalyst performance have included modifying the catalyst support, composition, structure, and loading.[2–4] One emerging approach to improving electrocatalyst performance and long-term durability is applying ultrathin oxide coatings directly to the surface.[5–8] Within this oxide-encapsulated electrocatalyst (OEC) architecture, electrocatalytic reactions can occur at the buried interface between the overlayer and encapsulated electrocatalyst if the overlayer is permeable to reactant and product species. When properly designed, oxide overlayers can improve electrocatalyst stability, activity, and durability for a wide range of electrocatalytic reactions.[9,10]

Many insights into the functionalities of semipermeable oxide encapsulation layers have been gained through studies of model thin film electrodes for which the structure and composition of the oxide overlayer can be precisely tuned.[6,8,11] For example, thin film Pt electrocatalysts encapsulated with ultrathin (2-10 nm) SiO_x (silicon oxide) overlayers were found to favor the oxygen evolution reaction (OER) over the chlorine evolution reaction (CER) in acidic and pH-neutral seawater, relative to a bare Pt control.[10] These improvements have been ascribed to the SiO_x overlayer being selectively impermeable to Cl^- ions, thus preventing their ability to access the buried Pt sites. Furthermore, SiO_x/Pt thin film electrodes have also exhibited enhanced activity for the methanol oxidation reaction (MOR)[7] and the ability to selectively permit the hydrogen evolution reaction (HER) while suppressing the O_2 reduction reaction.[12,13] By varying the synthesis

conditions of carbon-modified silicon oxide (SiO_xC_y) overlayers, Beatty et al. were able to show that the composition and structure of oxide overlayers can be tuned to control the relative fluxes of O_2 and H^+ to electrocatalyst active sites thanks to the different transport mechanisms of O_2 and H^+ within the oxide.[11] Although these model thin film electrodes are useful for correlating the thickness and composition of oxide overlayers with their transport properties and OEC performance, high surface area porous electrodes are necessary for industrially relevant applications.

The first challenge of applying nanoscopic oxide coatings to porous electrodes is preparing conformal coatings on complex 3-D structures. Atomic layer deposition (ALD) is one well-known method for depositing thin oxide layers on porous substrates[14], but its application to porous electrodes faces several challenges, including inconsistent film growth rates on porous surfaces, limited choice of precursors, and relatively high cost.[15] Takenaka et al. demonstrated the application of uniform silica layers onto Pt nanoparticles supported on carbon nanotubes (CNTs) and Ketjen black (KB) by successive hydrolysis and polycondensation of 3-aminopropyltriethoxysilane (APTES) and tetraethoxysilane (TEOS) as well as APTES and methyltriethoxysilane (MTEOS).[16–18] They achieved control over the diameter of the micro-pores within the layers by incorporating $NH_2–(CH_2)_n–NH_2$ (n = 6, 8, and 10) during the synthesis process[19] and enhanced stability, durability, and catalyst activity when the coated Pt/CNT and Pt/KB were tested in a polymer electrolyte fuel cell (PEFC).[18–21] These methods, while effective, involve multiple steps, such as preparing the catalyst ink, which requires the addition of ionomers to enhance the adhesion of the coated particles onto the substrate.[22,23]

A more streamlined approach would apply the oxide coating directly to catalyst-supported porous electrodes in a way that completely avoids the need for ionomers. One attractive method

for achieving this structure is the recently developed condensed layer deposition (CLD) process,[24–28] which shares some similarities with sol-gel processes commonly used to make oxide nanoparticles and coatings.[29] In sol-gel synthesis of oxide materials, metalorganic precursors dissolved in a solvent undergo hydrolysis reactions to form a solution of colloidal particles, forming a biphasic gel that can be applied to a substrate to produce a coating.[29–31] In contrast, CLD avoids the formation of colloidal particles in the bulk solution, instead carrying out hydrolysis of the metalorganic precursor directly on the surface of the target substrate. This surface-confined hydrolysis process is enabled by forming a thin nanoscopic water film on the substrate surface before introducing the metalorganic precursor. This leads to dense, conformal oxide coatings while minimizing hydrolysis in the bulk organic solvent.[24–27] Furthermore, Jasmin et al. showed that varying the thickness of the water film during the CLD process can be used to control the thickness of oxide layers deposited on nanoparticle substrates with nanometer-level precision.[24] In the current study, we extend the use of CLD to deposit nanoscopic titanium dioxide (TiO_2) overlayers on high surface area platinum nanoparticle catalysts supported on monolithic porous carbon foam (CF) substrates (Figure 1). TiO_2 was chosen as the overlayer material for this study owing to its excellent chemical stability over a wide range of pH conditions[32], low toxicity[33], and previous successful uses of TiO_2 as the overlayer material in oxide-encapsulated electrocatalysts.[25,34,35]

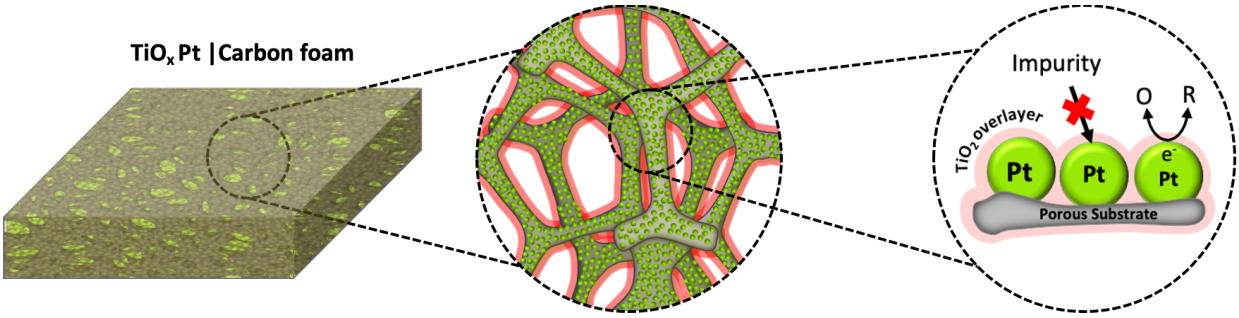

Figure 1. ***Rendering of titanium oxide (TiO_2)-coated platinized carbon foam (CF) electrodes,*** *where the pink layer, green dots, and grey substrate represent the TiO_2 overlayer, platinum nanoparticles, and porous carbon foam support material, respectively. The inset illustrates the basic operating process of TiO_2/Pt/CF electrode.*

In contrast to previously reported uses of CLD, this study uses the CLD method to directly deposit oxide overlayers onto the entire electrode structure (catalyst + support) rather than isolated catalytic nanoparticles or support/binder material. A potential advantage of adopting this approach is that depositing the catalytic nanoparticle first ensures a satisfactory electrical contact between the catalyst and substrate, avoiding interfacial resistance that could arise between an oxide-encapsulated electrocatalyst nanoparticle and a support material. As illustrated in Figure 2, this process consists of submerging a Pt/CF electrode into a non-polar hydrophobic solvent (heptane) and adding water, which condenses on the surface of the electrode if the electrode is more hydrophilic than the solvent.[24] Next, a metalorganic precursor such as titanium (IV) ethoxide (TEO) is added to the reaction solution, where it hydrolyzes to form TiO_2 when it contacts the water film on the surface of the electrode (Equation 1). As the surface-confined water is the limiting reagent for the hydrolysis reaction, the thickness of the coating is determined by the thickness of the nanoscopic H_2O film on the substrate material. Based on this understanding, enhancing the hydrophilicity of the substrate by creating surface functional groups should result in a more uniform coating.[24–27] Xing et al. reported that sonicating carbon nanotubes in 3 M H_2SO_4 + 0.1M HNO_3 at 60 °C for 2 hours significantly increased the oxygen content on the surface of the

nanotubes without major structural damage compared to samples treated for more extended periods.[36,37] Based on these observations, a surface functionalization step (Figure 2, Step 1) was applied in the current study to the CF substrate before Pt electrodeposition, in order to make the surface of the carbon foam more favorable for the formation of a uniform water film during the CLD process. To prevent water from the surface functionalization and electrodeposition steps from affecting the subsequent CLD steps, samples were thoroughly dried overnight and under high vacuum ($<6 \times 10^{-8}$ Torr) at 90°C for 1 hour prior to the CLD process.

$$Ti(OC_2H_5)_4 + 2H_2O \rightarrow TiO_2 + 4C_2H_5OH \quad (1.)$$

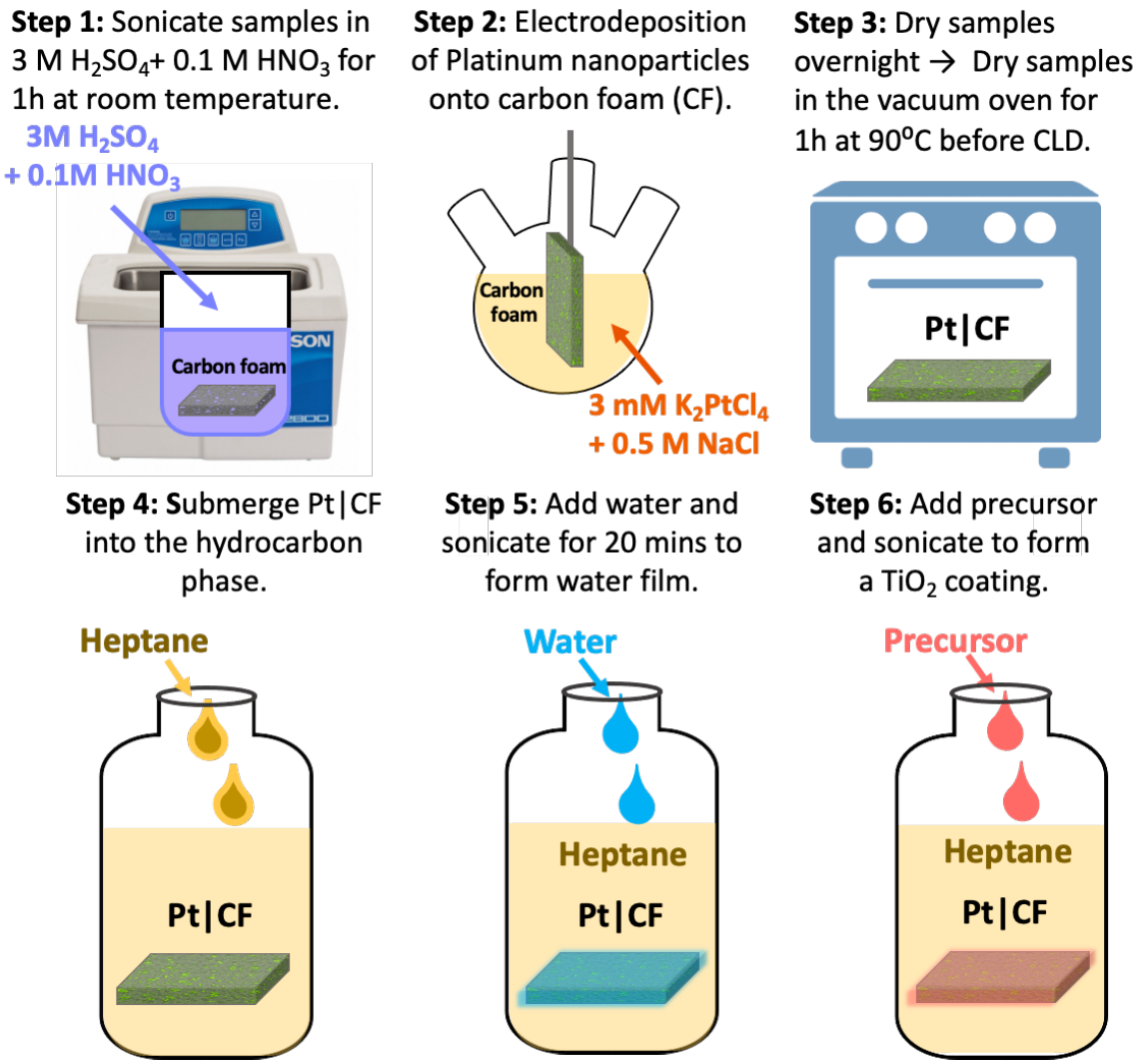

Figure 2. Key steps involved in the ***synthesis of TiO_2 -encapsulated platinized carbon foam (Pt/CF) electrodes by CLD.*** *This process was adapted from the CLD process described by Jasim et al.*[24]

Oxide overlayers deposited on porous electrodes via CLD can still exhibit non-uniformities, holes, or cracks. Such variations will likely give rise to different local selectivities, undesirable concentration overpotentials, and varying current densities across the electrode. Thus, this paper explores how varying the amounts of added precursor and water impacts the continuity and uniformity of the coating. After carrying physical characterization of the as-made electrodes with scanning electron microscopy (SEM), electron energy loss spectroscopy (EELS),

transmission electron microscopy (TEM), and X-ray photoelectron spectroscopy (XPS), the nature of the TiO_2 coatings was also probed by electroanalytical methods. Specifically, hydrogen underpotential deposition (H_{upd}) and carbon monoxide stripping voltammetry were used to evaluate the electrochemically active surface area of encapsulated electrodes, while, copper underpotential deposition (C_{upd}) measurements were used to assess the percentage of Pt sites covered by the TiO_2 overlayer.

II. Methodology

Chemicals – All solutions were prepared using 18.2 MΩ-cm deionized (DI) water, concentrated sulfuric acid (Certified ACS plus, Thermo Fisher Scientific), nitric acid (HNO_3, Certified ACS plus, Fisher Chemical ™), sodium chloride (ACS Reagent grade, Sigma-Aldrich), potassium tetrachloroplatinate (99.99% trace metal basis, Sigma-Aldrich), and copper sulfate ($CuSO_4$, Sigma-Aldrich, ReagentPlus), and purged with nitrogen gas (N_2, Purity Plus 99.999% purity) and carbon monoxide (CO, Purity Plus 99.999% purity) as required by electrochemical experiments. The precursor was prepared with heptane (HPLC, ≥ 96% Fisher Chemical™) and titanium (IV) ethoxide (TEO, technical grade, Sigma Aldrich).

Electrode fabrication - Electrodes were fabricated using porous conductive carbon foam (PCCF) characterized by 100 pores per inch (PPI) and sheet resistance of $7.82 \times 10^{-2}\ \Omega\ \text{square}^{-1}$ (McMaster-Carr). The electrode was cut into a 1 cm × 2.5 cm rectangle. The portion of the electrode tested was a rectangle of 1 cm × 1.5 cm with a thickness of 1.8 mm, while the portion of the electrode used as the electrical feedthrough remained at the original thickness of 5 mm. An electrical connection to the carbon foam was made by inserting a piece of titanium foil into the thicker

segment of the electrode. See EIS Section I Figure S1. The planar silicon (Si) wafer electrodes were coated with 2 nm of Ti at 0.5 Å s^{-1} and 5 × 10^{-6} Torr followed by 50 nm of Pt (99.99%) via electron-beam (e-beam) evaporation at 1 Å s^{-1} and 5 × 10^{-6} Torr.

Electrodeposition of platinum nanoparticles - Electrodes were sonicated in isopropanol, methanol, and DI water for 5 minutes each to remove impurities from the surface. The electrodes were then submerged in a 3 M H_2SO_4 + 0.1 M HNO_3 solution and sonicated for 1 hour at room temperature. The electrodes were rinsed thoroughly with DI water, and they underwent a two-step chronoamperometry (CA) procedure of 5 seconds each in a deaerated 0.5 M H_2SO_4 liquid electrolyte to further clean the surface of the electrode. The applied potential of the first CA step was 0.4 V vs. Ag/AgCl, and the second CA was -0.8 V vs. Ag/AgCl. Platinum nanoparticle electrocatalysts were deposited to the electrodes by carrying out cyclic voltammetry (CV) at 100 mV s^{-1} in a 3 mM K_2PtCl_4 + 0.5 M NaCl electrolyte (pH = 2.60) for 21 cycles between -0.7 V vs. Ag/AgCl and + 0.3 V vs. Ag/AgCl while stirring at 200 RPM.

Electrochemical surface area - After electrodeposition, the electrochemical surface area of electrodes was quantified by integrating the hydrogen underpotential adsorption and desorption features recorded during cyclic voltammetry (CV). Each electrode was cycled from 0.05 V vs. RHE to 1.2 V vs. RHE at 20 mV s^{-1} in a 3-neck round bottom flask where a carbon rod was the counter electrode (CE) and Ag/AgCl was the reference electrode. The electrochemical surface area (ECSA) was calculated by integrating the hydrogen underpotential deposition (H_{upd}) signal, correcting for double-layer capacitance, and using the specific capacitance of H_{upd} on polycrystalline Pt of 210 μC cm^{-2}_{Pt}.[38,39]

Condensed layer deposition - Following electrodeposition and the electrochemical characterization, the samples were dried overnight for 12 hours inside the fume hood. To further ensure that no water from previous steps was present during CLD, the samples were dried in a vacuum oven for 1 hr at 60 °C. The dried Pt/CF was submerged in 20 mL of heptane in a 60 mL Nalgene bottle. The total surface area of the porous electrode was calculated using its volume and the area/volume factor provided by the manufacturer for 100 PPI carbon foam of 2000 ft^2/ft^3.[40] The Nalgene bottle containing heptane + water was mounted inside the fume hood, and the probe sonicator (QEX 750) was introduced through a hole (diameter, 0.7 cm) that was drilled on the lid. To prevent moisture from reaching the sample, a plastic pipette was introduced to continuously purge the headspace with N_2 through a small hole punctured on the side of the bottle. The samples in the heptane + water mixture were sonicated for 20 minutes at an amplitude of 27% and an on-and-off pulses of 5 seconds and 1 second, respectively. Once the first sonication step was finished, a stoichiometric amount of ~ 0.2 M titanium (IV) ethoxide in heptane solution was added using a syringe. Due to the high volatility of heptane, the evaporated solvent in the bottle was replenished before starting the second sonication step. The samples in heptane + water + TEO solution were sonicated for 10 minutes under identical conditions as the first step. Finally, the samples were carefully removed, placed in a glass petri dish, and dried overnight inside the fume hood. Dried samples were stored in separate vials. In the case of planar samples, the surface activation process was skipped to avoid harming the Pt and Ti layers during the harsh acidic sonication bath. The preparation steps for these samples were the same as those for porous samples. To increase the total surface area, a dummy carbon foam measuring 1 cm × 1 cm × 0.5 cm was introduced into the Nalgene bottle to increase reagent quantities to larger and, therefore more workable volumes.

Materials characterization **–** Scanning electron microscopy (SEM) images and energy-dispersive X-ray spectroscopy (EDS) elemental maps were obtained using a Zeiss Gemini 500 instrument and a Zeiss Sigma VOP microscope. Accelerating voltages ranged from 5 kV to 12 kV. EDX elemental mapping and selected area electron diffraction (SAED) pattern on corresponding TiO_2-encapsulated carbon form were collected with an FEI TALOS F200X transmission/scanning transmission electron microscope (S/TEM) equipped with a high angle annular dark field (HAADF) detector and a CCD camera at 200 kV. TiO_2-coated platinum thin films deposited on silicon wafers were cross-sectioned and prepared using Thermo Fisher Helios G4 UX Focused Ion Beam milling by applying a protective layer of carbon using a Sharpie pen, followed by the deposition of a platinum (Pt) layer through ion beam deposition, see ESI Figure S2. The Scanning Transmission Electron Microscopy (STEM) measurements were performed using Thermo-Fisher FEI Spectra 300 TEM with ultra-high-brightness cold field emission gun (C-FEG) and spherical aberration correction ("Kraken" at Cornell University). The STEM resolution was 58 pm with probe current at 75 pA and 300 kV. The high-annular angle dark field (HAADF) image was collected with a C_2 aperture of 70 µm, camera length of 94 mm, and convergence angle of 30 mrad. The HAADF image stacks were taken with 2048 × 2048 pixels with 5 µs dwell time. The EELS data were recorded using a Continuum CMOS camera with an energy dispersion of 0.3 eV per channel. Cornell Spectrum imaging tool was used to process the EELS data from images.[41] X-ray photoelectron spectroscopy measurements were conducted in a PHI-5600 spectrometer with an Al-K alpha X-ray source. The scan rate was 0.05 eV s^{-1} with a pass energy of 23 eV. Ti 2p, O 1s, and Pt 4f spectra were calibrated with metallic Pt $4f_{7/2}$ at 71.1 eV.[11,42] The peak deconvolution was performed by identifying the Ti 2p and O 1s peaks associated with TiO_2[43] and surface oxygen species.[44]

Electrochemical measurements – All electrochemical measurements were conducted using a SP-200 BioLogic potentiostat. For all standard three-electrode measurements, a carbon rod (Saturn Industries) was used as the counter electrode, and an Ag|AgCl/sat. 3 M KCl ($E° = 0.21$ V vs NHE, Hach, E21M002) as the reference electrode, and Pt/CF and TiO_2/Pt/CF as the working electrode. Solutions were deaerated with nitrogen (N_2, Purity Plus 99.999% purity) at 1 atm pressure, and the pH was measured using a benchtop pH meter (Fisherbrand™ accumet™ AE150 Benchtop pH Meter) that was calibrated using pH buffer 1.68, 4.01, and 7.0. Carbon monoxide (CO) oxidation experiments were conducted by first measuring the background signal in deaerated 0.5 M H_2SO_4 during cyclic voltammetry (CV) for 3 cycles at 20 mV sec^{-1} from 0.4 V vs. RHE to 0.01 V vs. RHE to 1.2 V vs. RHE. CO was adsorbed to the surface of the electrode by saturating the electrolyte with $CO_{(g)}$ for 10 minutes at 400 RPM while holding the electrode at a potential of 0.05 V vs. RHE. The excess CO was removed by purging the headspace of the three-neck flask with N_2 for 10 minutes at 400 RPM and an applied potential of 0.05 V vs. RHE. To "strip" the CO, the stirring was stopped, and a CV from 0.4 V vs. RHE to 0.01 V vs. RHE to 1.2 V vs. RHE at 20 mV sec^{-1} was applied. To ensure that all CO was removed from the surface of the electrode, an additional two CVs at equal conditions were conducted. To quantify the platinum nanoparticles where CO was adsorbed, the difference between the integrated charge passed by the first and third CV was calculated and converted using the known factor of 420 μC cm^{-2}_{Pt}.[45]

Copper stripping experiments were performed in a well-stirred (200 RPM) three-neck flask in deaerated 0.5 M H_2SO_4. The background signal was measured via linear sweep voltammetry (LSV) from 0.38 V vs. RHE to 1 V vs. RHE at 20 mV sec^{-1}. Following the first LSV, 2 mM of copper sulfate ($CuSO_4$) were added to the 0.5 M H_2SO_4 supporting electrolyte contained in the three-neck flask. The 0.5 M H_2SO_4 + 2mM $CuSO_4$ solution was stirred thoroughly purged with

N_2, and the pH was measured before reintroducing the working electrode. Three consecutive measurements were carried out, starting with an LSV from 0.38 V vs. RHE to 1 V vs. RHE at 20 mV sec^{-1}, followed by a chronoamperometry (CA) at 0.38 V vs. RHE for 5 minutes, and a final LSV from 0.38 V vs. RHE to 1 V vs. RHE at 20 mV sec^{-1}. The background signal was subtracted from the copper stripping LSV, and the amount of Pt nanoparticles where Cu^{2+} ions deposited was quantified by integrating the Cu_{upd} signal and using the known conversion factor of 420 μC cm^2_{Pt}.[45]

III. Results and Discussion

3.1 Physical Characterization

TiO_2/Pt/CF samples were prepared by CLD as described in the introduction and methods section. Briefly, samples with varying amounts of TiO_2 were fabricated by adding varying quantities of water (3.4 μL, 4.90 μL, and 9.8 μL) to the reaction vessel, followed by the addition of TEO to trigger the TiO_2-forming hydrolysis reaction shown in Equation 1. To promote the complete conversion of water to TiO_2, 10% excess TEO was added compared to the stoichiometric amount required according to Equation 1 (H_2O:TEO = 2:1). Throughout this paper, samples are labeled as "low", "medium", and "high", to refer to the relative quantity of H_2O used during the CLD process. Based on previous studies employing CLD on nanoparticle substrates,[24] increasing the amount of H_2O relative to the surface area of the substrate leads to thicker TiO_2 coatings.

Substrate materials and TiO_2-encapsulated electrodes were first characterized by SEM, with representative images provided in Figure 3 for surface functionalized bare carbon foam (Figure 3a), platinized carbon foam (Figure 3b), TiO_2-encapsulated carbon foam (Figure 3c, 3e, and 3g), and TiO_2-coated platinized carbon foam (Figure 3d, 3f, and 3h). As seen in Figure 3a, the carbon foam substrate consists of 50 μm to 90 μm thick interconnected strands of carbon that form

pores having diameters varying between 200 μm and 300 μm. In Figure 3b, the electrodeposited platinum formed a layer that covered a large percentage of the surface of the carbon foam, although clear gaps in the Pt layer are evident. After the TiO_2 coating was applied to the bare carbon foam, splotchy deposits appeared on its surface (Figure 3c, 3e, and 3g). These features are most evident when the CLD process is carried out using the "high" water concentration (Figure 3g). When the CLD process was applied to the platinized samples, there was no noticeable difference in morphology between the uncoated (Figure 3b) and coated Pt/CF (Figures 3d, 3f, and 3h). Energy-dispersive X-ray spectroscopy (EDS) images of "medium" TiO_2/Pt/CF samples (ESI Section III Figure S3) revealed a relatively uniform distribution of the titanium signal on the surface of the platinized electrode, while mapping of a "medium" TiO_2/CF sample also indicated the presence of Ti, O, and C (ESI Section III Figure S4).

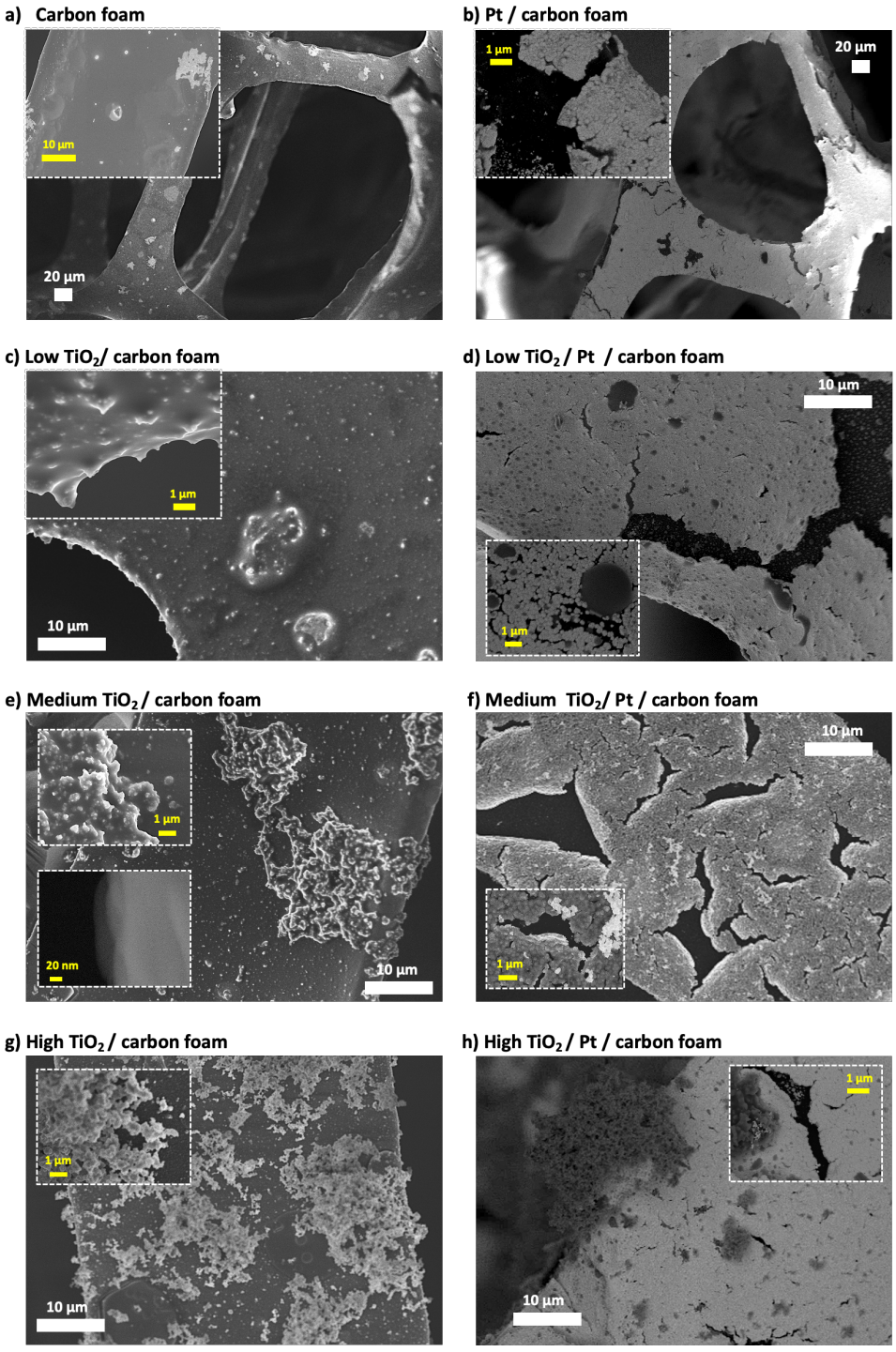

Figure 3. ***SEM images of coated and uncoated carbon foam and Pt/carbon foam.*** *The images show,* ***(a)*** *uncoated carbon foam,* ***(b)*** *Pt/coated carbon foam (Pt/CF), and carbon foam with* ***(c)*** *"low",* ***(e)*** *"medium", and* ***(g)*** *"high" water concentration used during CLD. Additionally,* ***(d, f, h)*** *show the corresponding Pt/carbon foam samples with the same water concentrations used during CLD process.*

To better characterize the nanostructure and chemical composition of the TiO_2 coatings, the coating process was also carried out under "medium" water concentration during CLD conditions to deposit TiO_2 onto smooth, 50 nm thick, platinum thin films supported on 2nm Ti + Si(100) substrate. In Figure 4a, a cross-sectional high-annular angle dark field (HAADF) image from the "medium" TiO_2/Pt/Si wafer confirms that the TiO_2 forms an overlayer on the Pt surface and indicates that the TiO_2 coating has a highly disordered structure, in contrast to the adjacent Pt layer. This was confirmed with selected area electron diffraction (SAED, ESI Section III Figure S4), which does not show a discernable diffraction pattern associated with crystalline TiO_2, indicating that the TiO_2 is disordered/amorphous.[46,47] EELS elemental maps captured on a different location of the same sample (Figure 4c-e) showed that the TiO_2 layer had a thickness that ranged between < 1 nm and 5 nm. Consistent with the literature for thin TiO_2 layers, Ti-$L_{2,3}$ edges seen in the EELS spectra (ESI Section III Figure S5)[48] were detected at approximately 455 eV, while the O-K edge appeared at 553 eV.[49] The single O-K edge is further evidence of the disordered nature of the TiO_2 overlayer.

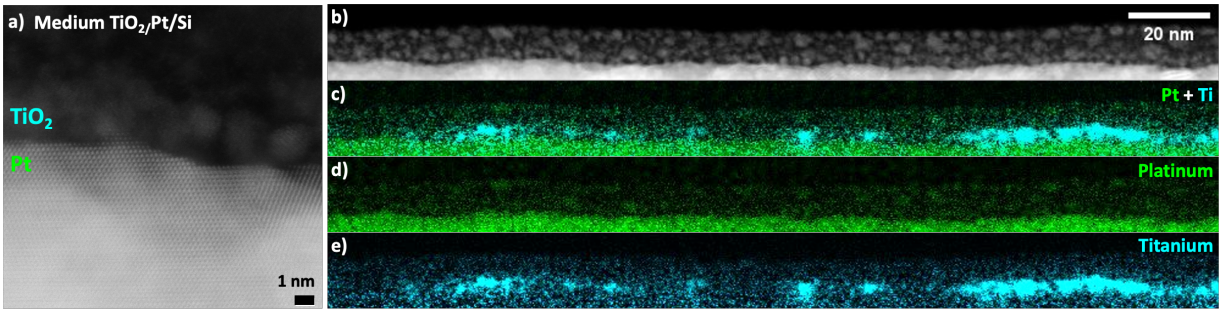

Figure 4. ***High-annular, dark field TEM images of TiO₂/Pt/Si*** *wafer samples for which the TiO_2 coating was deposited under a "medium" water concentration during CLD* ***(a, b, and f)****. EELS elemental mapping showing the* ***c)*** *Pt (green) + Ti (light blue),* ***d)*** *Pt (green), and* ***e)*** *Ti (light blue) distribution on the sample. See ESI Section III Figure S6 for extended EELS elemental mapping, including carbon and oxygen.*

X-Ray photoelectron spectra of a "medium" TiO_2/Pt/Si sample are compared to a bare Pt/Si control in Figure 5. For the bare Pt control sample, the peak center binding energies in the Pt 4f

spectra (Figure 5c) are consistent with the Pt thin film being present in the metallic Pt state (Pt^0),[6] while the minor O 1s signal appearing around 531.3 eV in Figure 5b can be attributed to adventitious oxygen species such as surface hydroxyls and adsorbed CO_2.[50] XPS results for the TiO_2/Pt/Si sample are shown in Figures 5d-5f. In Figure 5d, the Ti $2p_{1/2}$ and Ti $2p_{3/2}$ peak center binding energies of 464.3 eV and 458.7 eV are consistent with TiO_2,[51] which is further supported by finding a Ti:O ratio of 0.47 using the Ti 2p peak area and the lattice oxygen peak area at (530.3 eV) (ESI Section SIV Table S1). Oxygen species located at higher binding energy (≈ 532 eV) were deconvoluted from the lattice oxygen and included hydroxyl species, water, and adsorbed CO_2. Comparing the Pt 4f peaks of the bare Pt and TiO_2-encapsulated samples (Figures 5c and 5f), the Pt 4f peak locations are the same, but the intensity of the Pt 4f peak for the TiO_2/Pt/Si sample is attenuated by 16% due to screening of photoelectrons by the TiO_2 overlayer. The Pt 4f and Ti 2p peak areas were also used as inputs to an overlayer calculation (ESI Section IV Equation S1), which was used to estimate a TiO_2 overlayer thickness of 6.5 nm for the "medium" TiO_2/Pt/Si sample. This estimate is consistent with the observation from the TEM images and EELS maps in Figure 4. Overall, XPS results provided evidence that an ultrathin TiO_2 encapsulation layer was successfully applied over the metallic Pt/Si substrate.

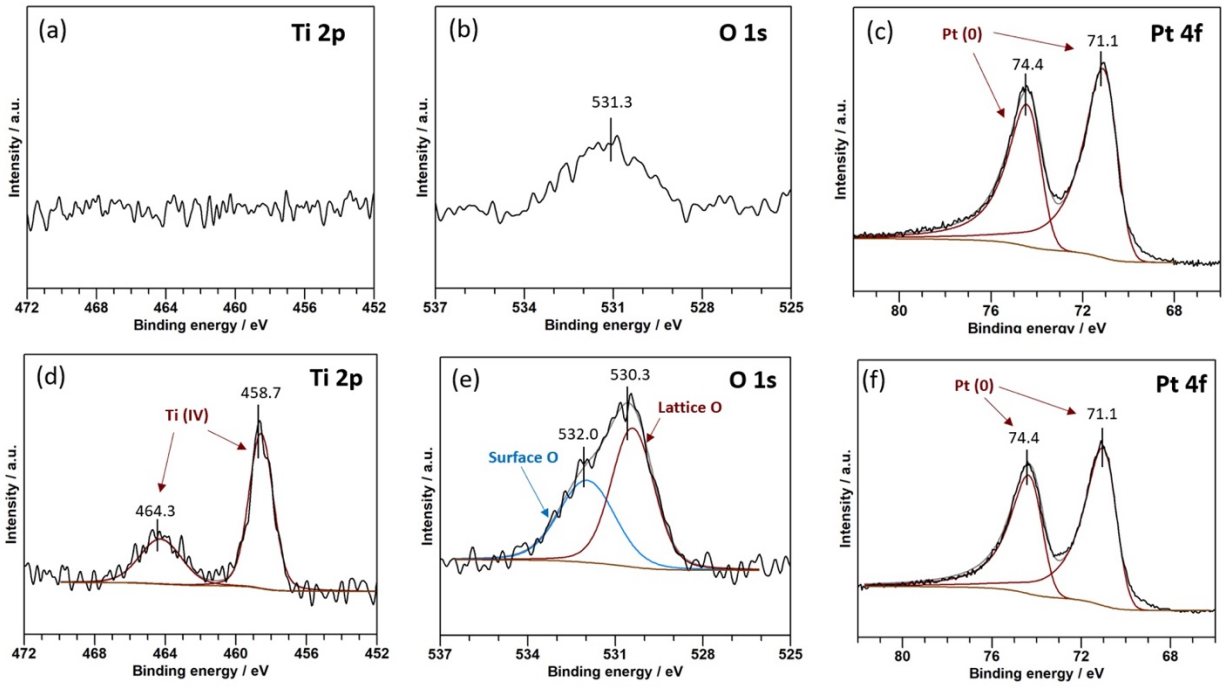

Figure 5. ***XPS characterization of thin film electrodes***. ***(a)*** *Ti 2p,* ***(b)*** *O 1s,* ***(c)*** *Pt 4f spectra of the bare Pt/Si electrode; and* ***(d)*** *Ti 2p,* ***(e)*** *O 1s,* ***(f)*** *Pt 4f spectra of a TiO_2-encapsualted Pt/Si electrode fabricated using the "medium" water concentration during CLD process. The y-axis ranges for the Ti 2p, O 1s, and Pt 4f spectra were kept the same between the two electrodes for easy comparison.*

3.2 Electrochemically Active Surface Area (ECSA)

The electrochemical surface area (ECSA) of Pt-based electrodes is commonly determined via hydrogen underpotential deposition (H_{upd}) measurements, whereby the charge associated with adsorption and desorption of a monolayer of hydrogen is used to quantify the total number of active sites.[39] Many studies have shown that cyclic voltammetry profiles for polycrystalline Pt from 0.05 V vs. RHE to 1.4 V vs. RHE show well-defined features of electro-adsorption and electro-desorption of H_{upd} as well as PtO_x formation and reduction.[39,52] When polycrystalline Pt electrodes are tested in sulfuric acid solutions, H_{upd} features are typically observed between 0.05 V vs. RHE to 0.35 V vs. RHE, while the signal associated with double layer capacitance dominates the CV profile from 0.40 V vs. RHE to 0.85 V vs. RHE. At more positive potentials, features

associated with Pt oxidation (PtO_x) are seen in the positive scan, and features associated with the reduction of those species are seen during the reverse scan.[39,52] As seen in Figure 6, CV curves for all bare Pt (grey dash lines) and TiO_2-encapsulated Pt/CF (solid lines) samples exhibit features associated with H_{upd} and PtO_x that are characteristic of polycrystalline Pt electrodes.[39,52] The ECSA of the bare Pt/CF and low, medium, and high TiO_2/Pt/CF electrodes were calculated by integrating the H_{upd} area, corrected for double layer capacitance, and using the specific capacitance of H_{upd} on polycrystalline Pt of 210 μC cm^{-2}_{Pt}.[39] The normalized ECSA for which the electrochemically active surface area has been normalized by the geometric surface area, also known as area per area factor, ranged from 55.7- 270.7 cm^2_{geo} cm^{-2}_{Pt}.

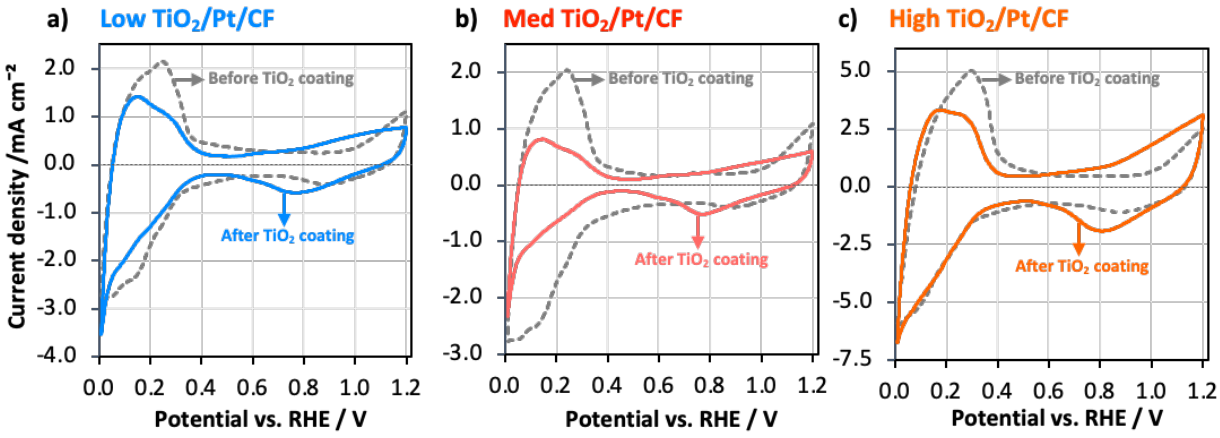

Figure 6. ***Hydrogen underpotential deposition (H_{upd}) cyclic voltammetry*** *measurements carried out at 20 mV sec^{-1} from 0.05 V vs. RHE to 1.2 V vs. RHE in deaerated 0.5 M H_2SO_4 before (dash lines) and after (solid lines) coating each Pt/CF electrode with TiO_2 using a* ***a)*** *"low",* ***b)*** *"medium", and* ***c)*** *"high" water concentration during CLD. The 3rd CV cycle out of three total CV cycles is shown for each electrode.*

The presence of notable H_{upd} features for all TiO_2/Pt/CF electrodes indicates that protons were able to travel through the TiO_2 overlayer and reach the buried TiO_2/Pt interface. Nonetheless, the decrease in the magnitude of the H_{upd} features observed in the CVs after TiO_2 coating (solid lines) indicates some loss in electrochemical surface area (Figure 6). Coated samples exhibited an

average of 46% ± 12 % decrease in H_{upd}-derived ECSA. Possible explanations include detachment and/or agglomeration of some platinum particles from the support during CLD or blocked active sites caused by regions of the electrode that are encapsulated by thicker coatings or particulate deposits (see ESI Section V Figure S7), which could significantly suppress the ability of the buried interface in these regions to access H^+ and be in ionic communication with the electrolyte.

Besides affecting H_{upd} signal, the addition of the CLD TiO_2 coating significantly alters the Pt oxidation redox features in the CV profiles of Figure 6. Most notably, the presence of the TiO_2 coating is observed to shift the onset for Pt oxidation between - 200 mV to -230 mV compared to that observed for bare Pt, which is seen to be around 0.85 V vs. RHE as expected. Additionally, increasing the water concentration during the CLD process resulted in a slightly less positive shift between 20 mV- 40 mV in the PtO_x onset potential. Previous work has claimed that negative shifts in the Pt oxidation onset potential can be caused by the ability of the overlayer to suppress sulfate adsorption, which competes with the formation of Pt-OH by blocking the adsorption of H_2O molecules.[7,53–55] Assuming this explanation applies the TiO_2/Pt electrodes studied here, the observed shifts in the PtO_x redox features provide further evidence that most of the Pt nanoparticles are successfully encapsulated by the TiO_2 layer.

The ECSAs of bare Pt and TiO_2/Pt electrodes were also measured by carbon monoxide (CO) stripping voltammetry, a technique that closely resembles H_{upd} but instead uses the oxidation of monolayer-levels of adsorbed CO to probe the number of active sites on the sample surface. As CO is also known as a catalyst poison in direct methanol fuel cells (DMFC), the location (i.e., peak potentials) of CO oxidation features recorded during CO stripping are also used to probe the tolerance of an electrocatalyst to this poison.[56] CO oxidation occurs on Pt through a Langmuir–

Hinshelwood reaction mechanism that involves a reaction between adsorbed CO (Equation 3) and adsorbed hydroxyls, the latter of which is formed electrochemically as shown in Equation 2. [57,58]

$$H_2O + Pt \rightarrow Pt\text{-}OH_{ads} + H^+ + e^- \quad (2.)$$

$$Pt\text{-}CO_{ads} + Pt\text{-}OH_{ads} \rightarrow CO_2 + H^+ + e^- + 2\ Pt \quad (3.)$$

In this work, CO was first adsorbed onto the surface of the electrode while purging the solution with CO and holding the potential at 0.05 V vs. RHE for 10 minutes. After removing dissolved CO from the bulk solution by purging with N_2 gas, the CO was "stripped" from the surface by sweeping the potential to positive (oxidizing) potentials.[59,60]

CO stripping voltammetry was performed on three different TiO_2-encapsulated Pt/CF electrodes and a bare Pt/CF control sample. Cyclic voltammetric profiles recorded before stripping (dotted grey lines), immediately after stripping (cycle 1, solid lines), and after 2 scans (cycle 3, dash lines) are presented in Figure 7. The bare Pt/CF sample exhibited a small shoulder at 0.62 V vs. RHE and a peak at 0.83 V vs. RHE (Figure 7a). H_{upd} features were observed during the third scan, indicating that all the CO was "stripped" from the electrode surface, allowing H^+ to adsorb onto the Pt. A larger peak for PtO_x was observed around 0.85 V vs. RHE after the CO was "stripped" from the surface compared to the background CV, which was conducted in deaerated 0.5 M H_2SO_4 before all electrochemical measurements. The CO oxidation peak centers recorded for the TiO_2/Pt/CF electrodes (0.74 - 0.78 V vs. RHE) were all lower than that recorded for the bare Pt/CF control sample (0.84 V vs. RHE). A pre-peak located ≈ 200 mV less positive than the primary CO oxidation peak was also observed for all coated samples.

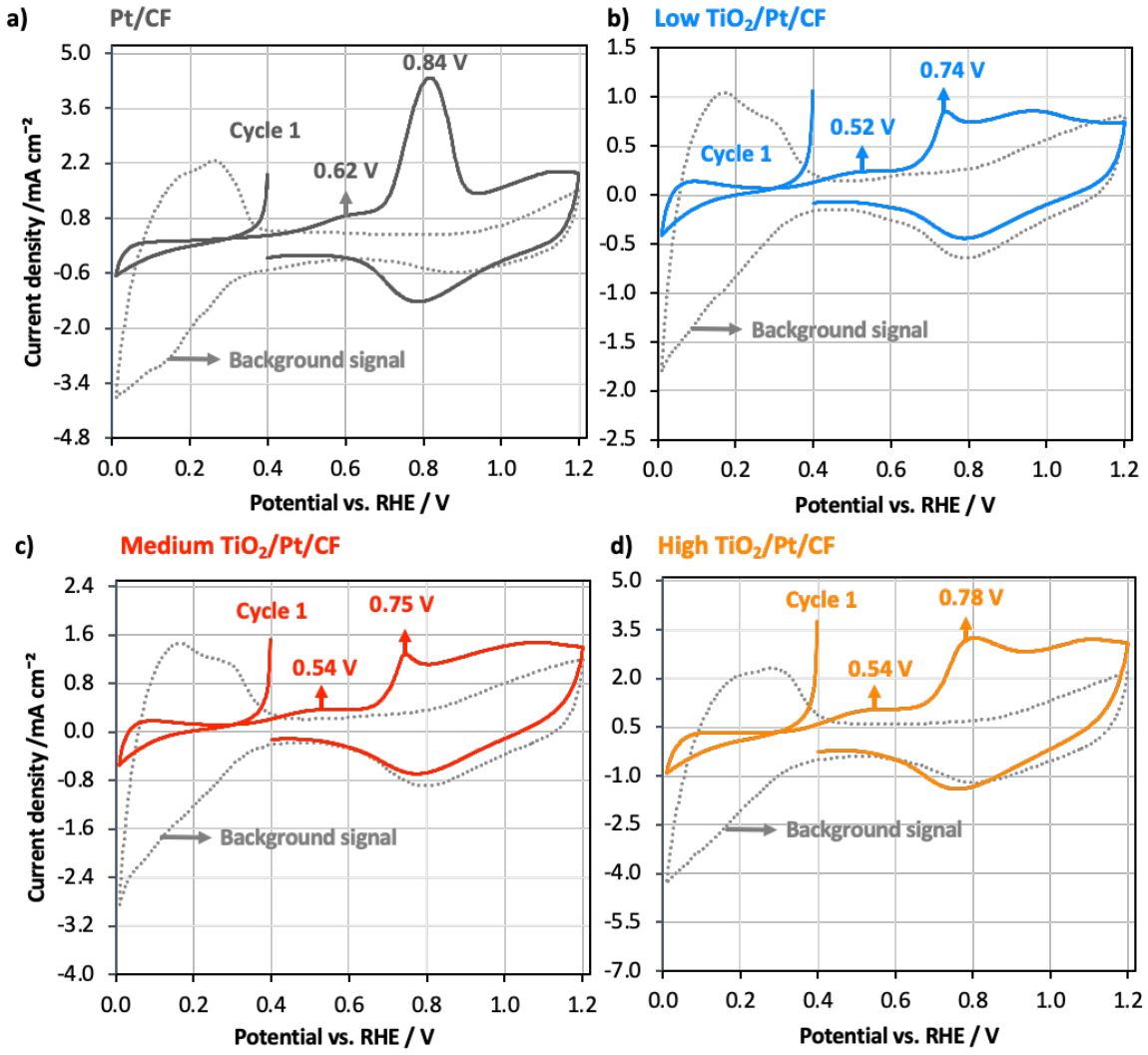

Figure 7. ***Carbon monoxide voltammetry*** *for Pt/CF electrodes fabricated using* ***(a)****, "low"* ***(b)****, "medium", and* ***(c)*** *"high" water concentrations during the CLD coating process. All CVs were conducted in deaerated 0.5 M H_2SO_4 at 20 mV s^{-1} from 0.01 V vs. RHE to 1.2 V vs. RHE. Background CV (grey dotted lines) were generated before CO poisoning, and cycle 1 (solid lines) immediately after CO poisoning.*

The locations of the CO oxidation peak and onset potentials observed for the bare Pt/CF sample are consistent with reported literature values.[61] The less positive onset and peak potentials for CO oxidation recorded for the low, medium, and high TiO_2/Pt/CF have also been observed in other studies for SiO_x-coated and TiO_2-supported Pt electrocatalysts.[7,62–64] Some of the possible explanations for this phenomena include: (i) an increased presence of more reactive lattice oxygen

in the TiO_2 overlayer promotes CO oxidation,[65] (ii) hydroxyl groups (e.g. silanols in SiO_x) present in the overlayer may help facilitate CO removal at lower overpotentials than required for Pt-OH-facilitated CO removal (Equation 3),[7] and (iii) strong interactions between Pt atoms bonded to Ti atoms in TiO_2, which can lower the activation energy for CO to adsorb onto the surface and can facilitate its diffusion.[66,67] Regardless of the exact mechanism, the less positive onset and peak potentials for CO oxidation can most likely be attributed to the presence of the TiO_2 overlayer and the microenvironment it creates at the TiO_2/Pt buried interface.

The lower CO oxidation onset potential for the encapsulated samples also suggests that the TiO_2 overlayer alters the energetics associated with CO binding to active sites at the buried interface compared to Pt atoms exposed to the bulk electrolyte. For example, steric influences associated with a nanoconfined environment at the buried interface might alter how the CO molecule coordinates with the Pt, which can change in orientation and impact its binding energy. Furthermore, the overlayer might alter the local electric field by changing the distribution of supporting electrolyte charges near the adsorbed CO molecules. Overall, the presence and nature of the CO stripping signal indicate that CO molecules can penetrate through the TiO_2 overlayer and be oxidized at active sites at the buried interface.

3.3 Cu stripping voltammetry

A second underdeposition method, copper stripping voltammetry, was also used to assess ECSA and further quantify the coverage of Pt by the TiO_2 overlayers. As shown in Equation 4, copper stripping is based on underpotential deposition of Cu^{2+} ions onto the Pt surface. The adsorbed underpotentially deposited Cu atoms (Cu_{upd}) are subsequently oxidized or "stripped" from the Pt nanoparticles by sweeping to more positive potentials. However, previous work has shown that dense oxide encapsulation layers are highly effective at blocking the relatively large solvated Cu^{2+}

ions from reaching the oxide/Pt interface.[8] Thus, for overlayers that completely block the transport of Cu^{2+} to the buried interface, the suppression in Cu_{upd} signal by encapsulated electrodes compared to bare Pt controls can be used to estimate the percentage of Pt active sites that remain exposed to the bulk electrolyte due to cracks, holes, or partial delamination of the oxide layer. This quantification is carried out by integrating the Cu_{upd} signal and using the known conversion factor of 420 μC cm^{-2} Pt for polycrystalline Pt.[45]

$$Cu^{2+} + 2\ e^- \leftrightharpoons C_{upd}, \qquad E^o = 0.34 \text{ V vs. SHE} \qquad (4.)$$

Cu stripping voltammetry measurements were carried out for bare Pt/CF and TiO_2/Pt/CF electrodes made with "low", "medium", and "high" water concentrations during the CLD process. First, the background signal for all samples was measured by carrying out linear swept voltammetry (LSV) from 0.38 V vs. RHE to 1.00 V vs. RHE at 20 mV s^{-1} in the Cu-free supporting electrolyte. After adding 2 mM copper sulfate to the supporting electrolyte, the electrode was held at an (under)potential of 0.38 V vs. RHE for 5 minutes to allow Cu^{2+} ions to adsorb onto exposed Pt sites. Immediately after, the Cu_{upd} ions were oxidized by sweeping the potential to 1.0 V vs. RHE at 20 mV s^{-1}. Both background and Cu stripping LSV curves are shown in Figure 8.

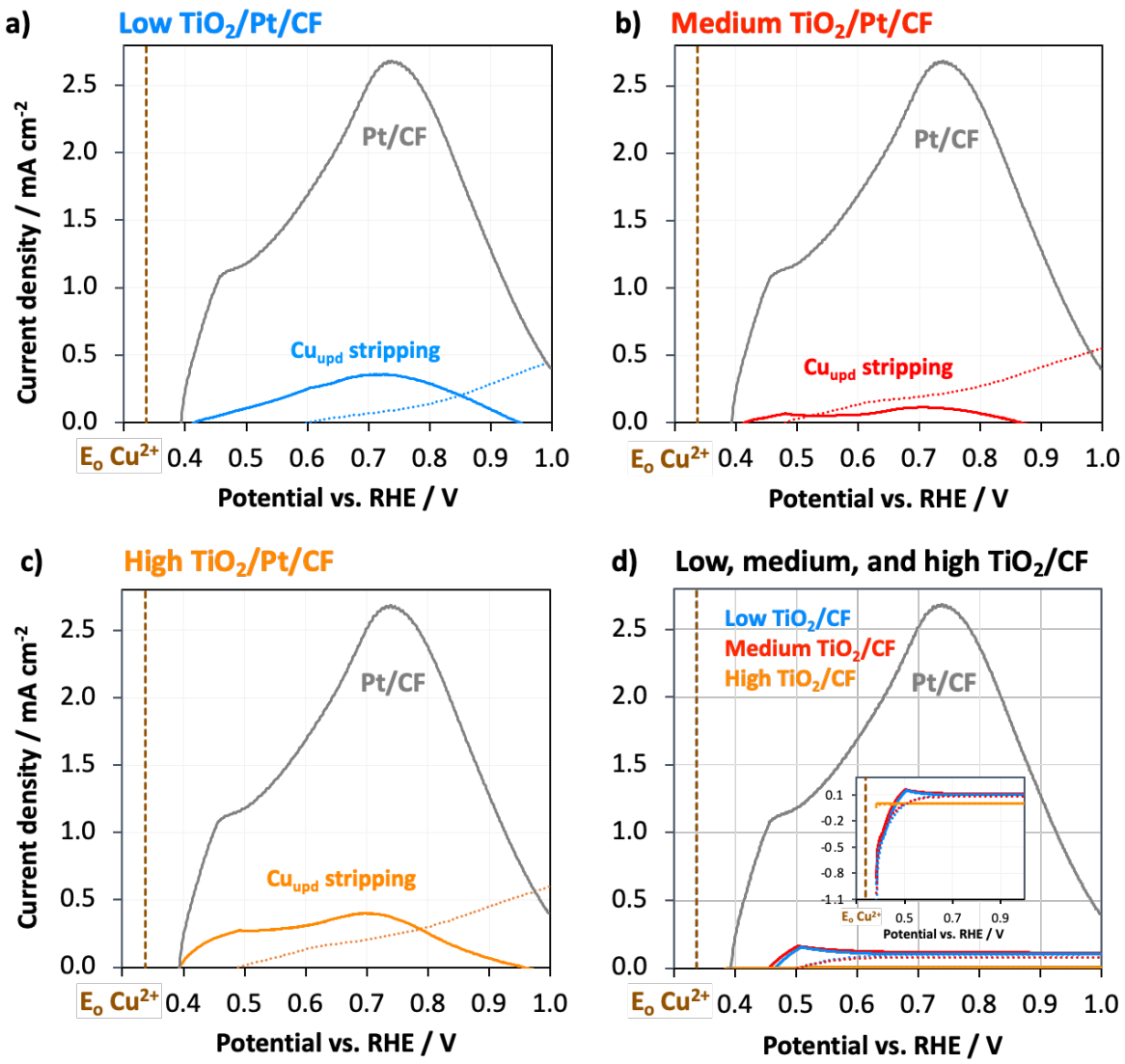

Figure 8. ***Copper stripping voltammetry*** *from 0.38 V vs. RHE to 1 V vs. RHE at 20 mV* s^{-1} *in deaerated and stirred 0.5 M* H_2SO_4 *+ 2 mM* $CuSO_4$ *for* ***a)*** *"low",* ***b)*** *"medium", and* ***c)*** *"high"* TiO_2*/Pt/CF as well as* ***d)*** *low, medium, and high* TiO_2*/CF. Grey solid lines and dotted LSVs indicate bare Pt/CF* Cu^{2+} *stripping and background signal in deaerated 0.5 M* H_2SO_4*, respectively. Background LSV (dotted lines) was subtracted from all* Cu_{upd} *LSVs (solid lines).*

In Figure 8, the copper stripping voltammetry curve for the bare Pt/CF electrode exhibits a distinct oxidation peak centered at ≈ 0.74 V vs. RHE and a shoulder at ≈ 0.46 V vs. RHE, which is similar to the results obtained in other studies for polycrystalline Pt.[6,68,69] In contrast, the TiO_2/Pt/CF electrodes show broad, shallow peaks in the background-subtracted Cu stripping

curves (Figure 8a-c), while TiO_2-coated CF control samples (Figure 8d) do not display any peaks. The negligible shift in Cu_{upd} oxidation peak potentials for the TiO_2/Pt/CF electrodes indicates similar binding energies to the bare Pt control sample, suggesting that Cu_{upd} signal is observed due to cracks and holes that expose Pt nanoparticles and not due to Cu_{upd} stripped from the TiO_2/Pt buried interface. It was also observed that varying the water concentration during CLD process, which in theory should result in different coating thicknesses, did not impact the transport of Cu^{2+} ions. This observation suggests that a similar TiO_2 coverage of Pt was observed for low, medium, and high TiO_2/Pt/CF. Lastly, the inset in Figure 8d shows a significant reduction current for the low and medium TiO_2/CF samples, possibly due to proton intercalation into the TiO_2 coating.[70]

To summarize the results from H_{upd}, CO stripping, and Cu stripping measurements, ECSAs obtained from each electroanalytical method were plotted in Figure 9. In this figure, the ECSAs (i.e. cm^2 of active Pt) were normalized to the geometric area of the electrode, and the CO stripping and Cu stripping ECSAs plotted vs. the H_{upd} ECSA. Important insights may be gained based on the location of experimental data points with respect to the dashed grey line, which represents perfect agreement in the CO stripping or Cu stripping-determined ECSA and the H_{upd}-determined ECSA. Focusing first on the data points for the bare Pt/CF electrode, ECSAs determined by Cu^{2+} and CO stripping overestimate H_{upd}-derived ECSA by 27-95% and 31%-49%, respectively. Previous studies have also reported that the Cu^{2+} and CO stripping methods overestimate the electrochemical surface area of bare Pt samples compared to H_{upd} methods, possibly due to uncertainties associated with capacitance charge correction or the selection of the lower potential limit.[71] However, the Cu^{2+} and CO stripping-derived ECSAs for the TiO_2/Pt/CF electrodes were 43-98% and 5-43% lower, respectively, than the H_{upd}-derived ECSAs. Only one TiO_2/Pt sample tested exhibited a CO stripping-derived ECSA larger than its H_{upd}-derived ECSA. While the

differences between the CO stripping and H_{upd} ECSAs are quite small, the significant discrepancy between the Cu stripping and H_{upd} measurements can be attributed to the suppressed transport of Cu^{2+} through TiO_2 coatings to reach the buried interface. If it is assumed that the TiO_2 coatings are completely impervious to Cu^{2+} and all Cu_{upd} signal is associated with unencapsulated Pt, then the difference between the H_{upd} and Cu_{upd}-derived ECSAs can be used to estimate the percentage of active Pt sites that have been successfully encapsulated by the CLD process. Applying these assumptions to the data in Figure 9, between 43-98% of the active Pt sites were covered with dense TiO_2 layers that block Cu^{2+}, implying that between 2-57% of sites still remained exposed to the bulk electrolyte. The range of coverages estimated based on Cu_{upd} and H_{upd}-derived ECSAs are in line with the partial coverages of coatings seen in representative TEM/EELS images of the planar samples (Figure 4, Figure S6).

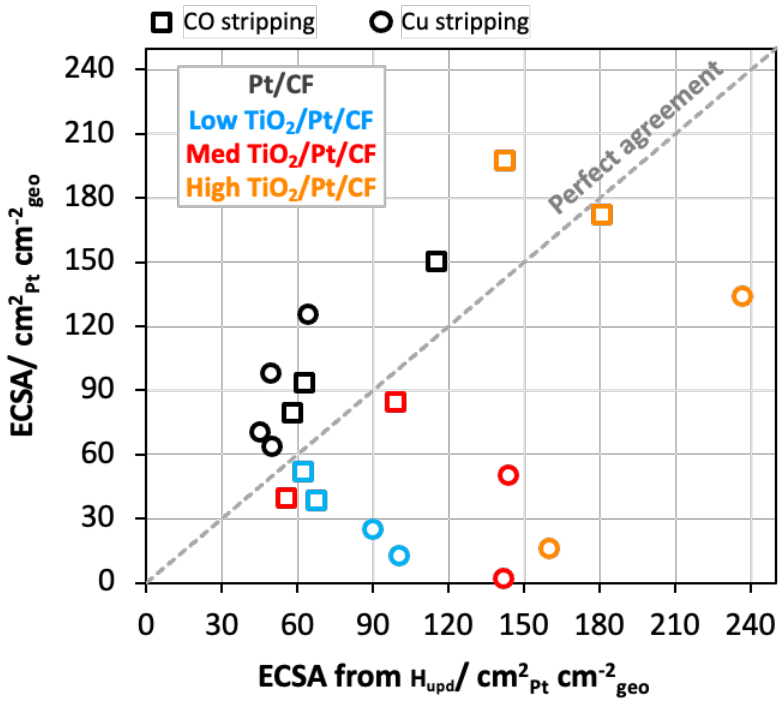

Figure 9. ***ECSAs measured from Cu_{upd} (circles) and CO oxidation (squares) signal as a function of area per area factor from H_{upd} signal.*** *Area per area factor for the low (blue), medium (red), and high (orange) TiO_2/Pt/CF samples as a function of H_{upd}. The dashed line represents the perfect agreement of area per area factors measured from Cu_{upd} or CO oxidation and H_{upd}.*

Conclusions

Condensed layer deposition (CLD) is a promising method for encapsulating porous electrodes with nanoscopic coatings. TEM, EELS, and XPS measurements confirmed that platinized carbon foam (Pt/CF) electrodes could be successfully coated with TiO_2 using the CLD process. Hydrogen underpotential deposition (H_{upd}) and carbon monoxide stripping measurements showed that Pt sites encapsulated by CLD TiO_2 coatings remain active, with minimal loss in electrochemically active surface area compared to bare Pt controls. Concurrently, these measurements revealed that H^+ and CO molecules are able to transport through the overlayer and reach the TiO_2/Pt buried interface. Less positive onset and peak potentials were observed for TiO_2/Pt electrodes during CO oxidation, indicating that the TiO_2/Pt active sites are characterized by altered binding environments compared to bare Pt sites exposed to the bulk electrolyte. In contrast to ECSAs derived from CO stripping measurements, the ECSAs of TiO_2/Pt determined from copper stripping voltammetry were substantially suppressed compared to H_{upd}-derived ECSAs, which was attributed to the ability of the TiO_2 coatings to block Cu^{2+} ions from reaching the active catalyst. Assuming the detected Cu_{upd} signal originates from exposed Pt, the difference between the Cu stripping and H_{upd} ECSAs was furthermore used to estimate the fraction of unencapsulated active Pt sites, which was found to be between 2–57%. Further optimization of the CLD process is necessary to minimize non-uniformities in coating coverage and thickness, which can lead to changes in local current densities, selectivity, and activity.

Acknowledgments

The authors would like to acknowledge the support of Qatar National Research Fund (a member of Qatar Foundation) through Grant # NPRP 12S-0215-190090. The findings achieved herein are solely the responsibility of the authors. The authors also acknowledge the co-funding provided by

Qatar Shell. The authors acknowledge staff support and instrumentation in the Columbia University clean room and shared materials characterization facilities. The authors thank Marshall Tekell (Columbia U.), Nicholas Mendez (Columbia U.), and Dr. Andrés Molina Villarino (Cornell U.) for helpful discussions and insights related to sample preparation and interpretation of characterization results.

References

(1) Mallapragada, D. S.; Dvorkin, Y.; Modestino, M. A.; Esposito, D. V; Smith, W. A.; Hodge, B.-M.; Harold, M. P.; Donnelly, V. M.; Nuz, A.; Bloomquist, C.; Baker, K.; Grabow, L. C.; Yan, Y.; Rajput, N. N.; Hartman, R. L.; Biddinger, E. J.; Aydil, E. S.; Taylor, A. D. Decarbonization of the Chemical Industry through Electrification: Barriers and Opportunities. *Joule* **2023**, *7* (1), 23–41. DOI:10.1016/j.joule.2022.12.008.

(2) Ramli, Z. A. C.; Kamarudin, S. K. Platinum-Based Catalysts on Various Carbon Supports and Conducting Polymers for Direct Methanol Fuel Cell Applications: A Review. *Nanoscale Res Lett* **2018**, *13* (1), 410. DOI:10.1186/s11671-018-2799-4.

(3) Nabil, Y.; Cavaliere, S.; Harkness, I. A.; Sharman, J. D. B.; Jones, D. J.; Rozière, J. Novel Niobium Carbide/Carbon Porous Nanotube Electrocatalyst Supports for Proton Exchange Membrane Fuel Cell Cathodes. *J Power Sources* **2017**, *363*, 20–26. DOI:10.1016/j.jpowsour.2017.07.058.

(4) Liu, Z.; Ma, L.; Zhang, J.; Kitiya, H.; Goodwin, J. G.; Hongsirikarn, K. Pt Alloy Electrocatalysts for Proton Exchange Membrane Fuel Cells: A Review. *Catalysis Reviews Science and Engineering* **2013**, *55* (3), 255–288. DOI:10.1080/01614940.2013.795455.

(5) Monai, M.; Jenkinson, K.; Melcherts, A. E. M.; Louwen, J. N.; Irmak, E. A.; Van Aert, S.; Altantzis, T.; Vogt, C.; van der Stam, W.; Duchoň, T.; Šmíd, B.; Groeneveld, E.; Berben, P.; Bals, S.; Weckhuysen, B. M. Restructuring of Titanium Oxide Overlayers over Nickel Nanoparticles during Catalysis. *Science (1979)* **2023**, *380* (6645), 644–651. DOI:10.1126/science.adf6984.

(6) Beatty, M. E. S.; Chen, H.; Labrador, N. Y.; Lee, B. J.; Esposito, D. V. Structure-Property Relationships Describing the Buried Interface between Silicon Oxide Overlayers and Electrocatalytic Platinum Thin Films †. **2018**. DOI:10.1039/c8ta06969g.

(7) Robinson, J. E.; Labrador, N. Y.; Chen, H.; Sartor, B. E.; Esposito, D. V. Silicon Oxide-Encapsulated Platinum Thin Films as Highly Active Electrocatalysts for Carbon Monoxide and Methanol Oxidation. *ACS Catal* **2018**, *8* (12), 11423–11434. DOI:10.1021/acscatal.8b03626.

(8) Labrador, N. Y.; Songcuan, E. L.; De Silva, C.; Chen, H.; Kurdziel, S. J.; Ramachandran, R. K.; Detavernier, C.; Esposito, D. V. Hydrogen Evolution at the Buried Interface between Pt Thin Films and Silicon Oxide Nanomembranes. *ACS Catal* **2018**, *8* (3), 1767–1778. DOI:10.1021/acscatal.7b02668.

(9) Esposito, D. V; Guilimondi, V.; Vos, J. G.; Koper, M. T. M. Chapter 7- Design Principles for Oxide-Encapsulated Electrocatalysts. In *Ultrathin Oxide Layers for Solar and*

Electrocatalytic Systems; Frei, H., Esposito, D., Eds.; The Royal Society of Chemistry, 2022; pp 167–207. DOI:10.1039/9781839163708-00167.

(10) Bhardwaj, A. A.; Vos, J. G.; Beatty, M. E. S.; Baxter, A. F.; Koper, M. T. M.; Yip, N. Y.; Esposito, D. V. Ultrathin Silicon Oxide Overlayers Enable Selective Oxygen Evolution from Acidic and Unbuffered PH-Neutral Seawater. *ACS Catal* **2021**, *11* (3), 1316–1330. DOI:10.1021/acscatal.0c04343.

(11) Beatty, M. E. S.; Gillette, E. I.; Haley, A. T.; Esposito, D. V. Controlling the Relative Fluxes of Protons and Oxygen to Electrocatalytic Buried Interfaces with Tunable Silicon Oxide Overlayers. *ACS Appl Energy Mater* **2020**, *3* (12), 12338–12350. DOI:10.1021/acsaem.0c02359.

(12) Bau, J. A.; Takanabe, K. Ultrathin Microporous SiO2 Membranes Photodeposited on Hydrogen Evolving Catalysts Enabling Overall Water Splitting. *ACS Catal* **2017**, *7* (11), 7931–7940. DOI:10.1021/acscatal.7b03017.

(13) Jo, W. J.; Katsoukis, G.; Frei, H. Ultrathin Amorphous Silica Membrane Enhances Proton Transfer across Solid-to-Solid Interfaces of Stacked Metal Oxide Nanolayers While Blocking Oxygen. *Adv Funct Mater* **2020**, *30* (12), 1909262. DOI:10.1002/adfm.201909262.

(14) Buabthong, P.; Ifkovits, Z. P.; Kempler, P. A.; Chen, Y.; Nunez, P. D.; Brunschwig, B. S.; Papadantonakis, K. M.; Lewis, N. S. Failure Modes of Protection Layers Produced by Atomic Layer Deposition of Amorphous TiO2 on GaAs Anodes. *Energy Environ Sci* **2020**, *13* (11), 4269–4279. DOI:10.1039/d0ee02032j.

(15) Onn, T. M.; Küngas, R.; Fornasiero, P.; Huang, K.; Gorte, R. J. Atomic Layer Deposition on Porous Materials: Problems with Conventional Approaches to Catalyst and Fuel Cell Electrode Preparation. *Inorganics 2018, Vol. 6, Page 34* **2018**, *6* (1), 34. DOI:10.3390/inorganics6010034.

(16) Takenaka, S.; Arike, T.; Nakagawa, K.; Matsune, H.; Kishida, M.; Tanabe, E. Synthesis of Carbon Nanotube-Supported Pt Nanoparticles Covered with Silica Layers. *Carbon N Y* **2008**, *46* (2), 365–368. DOI:10.1016/j.carbon.2007.11.011.

(17) Takenaka, S.; Arike, T.; Matsune, H.; Tanabe, E.; Kishida, M. Preparation of Carbon Nanotube-Supported Metal Nanoparticles Coated with Silica Layers. *J Catal* **2008**, *257*, 345–355. DOI:10.1016/j.jcat.2008.05.016.

(18) Park, K.; Goto, M.; So, M.; Takenaka, S.; Tsuge, Y.; Inoue, G. Influence of Cathode Catalyst Layer with SiO2-Coated Pt/Ketjen Black Catalysts on Performance for Polymer Electrolyte Fuel Cells. *Catalysts 2021, Vol. 11, Page 1517* **2021**, *11* (12), 1517. DOI:10.3390/catal11121517.

(19) Takenaka, S.; Miyazaki, T.; Matsune, H.; Kishida, M. Highly Active and Durable Silica-Coated Pt Cathode Catalysts for Polymer Electrolyte Fuel Cells: Control of Micropore Structures in Silica Layers. *Catal Sci Technol* **2015**, *5* (2), 1133–1142. DOI:10.1039/c4cy01301h.

(20) Takenaka, S.; Miyamoto, H.; Utsunomiya, Y.; Matsune, H.; Kishida, M. Catalytic Activity of Highly Durable Pt/CNT Catalysts Covered with Hydrophobic Silica Layers for the Oxygen Reduction Reaction in PEFCs. **2013**. DOI:10.1021/jp407928m.

(21) Takenaka, S.; Goto, M.; Masuda, Y.; Emura, S.; Kishida, M. Improvement in the Durability of Carbon Black-Supported Pt Cathode Catalysts by Silica-Coating for Use in PEFCs. *Int J Hydrogen Energy* **2018**, *43* (15), 7473–7482. DOI:10.1016/j.ijhydene.2018.02.159.

(22) Kobayashi, A.; Fujii, T.; Harada, C.; Yasumoto, E.; Takeda, K.; Kakinuma, K.; Uchida, M. Effect of Pt and Ionomer Distribution on Polymer Electrolyte Fuel Cell Performance and Durability. *ACS Appl Energy Mater* **2021**, *4* (3), 2307–2317. DOI:10.1021/acsaem.0c02841.
(23) Alink, R.; Singh, R.; Schneider, P.; Christmann, K.; Schall, J.; Keding, R.; Zamel, N. Full Parametric Study of the Influence of Ionomer Content, Catalyst Loading and Catalyst Type on Oxygen and Ion Transport in PEM Fuel Cell Catalyst Layers. *Molecules* **2020**, *25* (7). DOI:10.3390/molecules25071523.
(24) Jasim, A. M.; He, X.; White, T. A.; Xing, Y. Nano-Layer Deposition of Metal Oxides via a Condensed Water Film. *Communications Materials 2020 1:1* **2020**, *1* (1), 1–7. DOI:10.1038/s43246-020-0010-9.
(25) Jasim, Ahmed. M.; Al-Salihi, S.; Xing, Y. Communication—Platinum and Tin Oxide Dispersed in a Fluffy TiO2 Nanolayer for Electrocatalytic Reduction of Oxygen. *J Electrochem Soc* **2020**, *167* (11), 116526. DOI:10.1149/1945-7111/aba96c.
(26) Al-Salihi, S.; Jasim, A. M.; Fidalgo, M. M.; Xing, Y. Removal of Congo Red Dyes from Aqueous Solutions by Porous γ-Alumina Nanoshells. *Chemosphere* **2022**, *286*, 131769. DOI:10.1016/j.chemosphere.2021.131769.
(27) Jasim, A. M.; Xu, G.; Al-Salihi, S.; Xing, Y. Dense Niobium Oxide Coating on Carbon Black as a Support to Platinum Electrocatalyst for Oxygen Reduction. *ChemistrySelect* **2020**, *5* (37), 11431–11437. DOI:10.1002/slct.202003225.
(28) Xing, Y.; Jasmin, A. M. A Method of Forming Conformable Nanoscale Coatings on Substrates. WO2019140169A1, July 18, 2019.
(29) Xing, Y. Ultrathin Oxide Coatings Synthesized Via Wet Chemical Processes for Electrocatalytic Systems. In *Ultrathin Oxide Layers for Solar and Electrocatalytic Systems*; Frei, H., Esposito, D., Eds.; The Royal Society of Chemistry, 2022; p 0. DOI:10.1039/9781839163708-00236.
(30) Liang, Y.; Sun, S.; Deng, T.; Ding, H.; Chen, W.; Chen, Y. The Preparation of TiO 2 Film by the Sol-Gel Method and Evaluation of Its Self-Cleaning Property. *Materials (Basel)* **2018**. DOI:10.3390/ma11030450.
(31) Rajabi, N.; Wojcik, P. M.; Khanal, L. R.; Qiang, Y.; Mcilroy, D. N. A Comparison of the Morphological and Electrical Properties of Sol-Gel Dip Coating and Atomic Layer Deposition of ZnO on 3D Nanospring Mats. **2018**. DOI:10.1088/2053-1591/aaf440.
(32) Pourbaix, M. Titanium. In *Atlas of Electrochemical Equilibria in Aqueous Solutions*; NACE Foundation: Houston, 1974; pp 213–222.
(33) Fröschl, T.; Hörmann, U.; Kubiak, P.; Kucerová, G.; Pfanzelt, M.; Weiss, C. K.; Behm, R. J.; Hüsing, N.; Kaiser, U.; Landfester, K.; Wohlfahrt-Mehrens, M. High Surface Area Crystalline Titanium Dioxide: Potential and Limits in Electrochemical Energy Storage and Catalysis. *Chem Soc Rev* **2012**, *41* (15), 5313–5360. DOI:10.1039/c2cs35013k.
(34) Gu, J.; Yan, Y.; Young, J. L.; Steirer, K. X.; Neale, N. R.; Turner, J. A. Water Reduction by a P-GaInP2 Photoelectrode Stabilized by an Amorphous TiO2 Coating and a Molecular Cobalt Catalyst. *Nat Mater* **2016**, *15* (4), 456–460. DOI:10.1038/nmat4511.
(35) Finke, C. E.; Omelchenko, S. T.; Jasper, J. T.; Lichterman, M. F.; Read, C. G.; Lewis, N. S.; Hoffmann, M. R. Enhancing the Activity of Oxygen-Evolution and Chlorine-Evolution Electrocatalysts by Atomic Layer Deposition of TiO2. *Energy Environ Sci* **2019**, *12* (1), 358–365. DOI:10.1039/c8ee02351d.

(36) Xing, Y. Synthesis and Electrochemical Characterization of Uniformly-Dispersed High Loading Pt Nanoparticles on Sonochemically-Treated Carbon Nanotubes. *Journal of Physical Chemistry B* **2004**, *108* (50), 19255–19259. DOI:10.1021/JP046697I.
(37) Xing, Y.; Li, L.; Chusuei, C. C.; Hull, R. V. Sonochemical Oxidation of Multiwalled Carbon Nanotubes. *Langmuir* **2005**, *21* (9), 4185–4190. DOI:10.1021/la047268e.
(38) van der Vliet, D. F.; Wang, C.; Li, D.; Paulikas, A. P.; Greeley, J.; Rankin, R. B.; Strmcnik, D.; Tripkovic, D.; Markovic, N. M.; Stamenkovic, V. R. Unique Electrochemical Adsorption Properties of Pt-Skin Surfaces. *Angewandte Chemie International Edition* **2012**, *51* (13), 3139–3142. DOI:10.1002/anie.201107668.
(39) Jerkiewicz, G. Electrochemical Hydrogen Adsorption and Absorption. Part 1: Under-Potential Deposition of Hydrogen. *Electrocatalysis* **2010**, *1* (4), 179–199. DOI:10.1007/s12678-010-0022-1.
(40) *Carbon Foam | RVC Foam | Open Cell Foam | Reticulated Foam*. https://ergaerospace.com/carbon-rvc-foam-open-cell-material/ (accessed 2022-07-13).
(41) Cueva, P.; Hovden, R.; Mundy, J. A.; Xin, H. L.; Muller, D. A. Data Processing for Atomic Resolution Electron Energy Loss Spectroscopy. *Microscopy and Microanalysis* **2012**, *18* (4), 667–675. DOI:10.1017/S1431927612000244.
(42) Hatanaka, M.; Takahashi, N.; Takahashi, N.; Tanabe, T.; Nagai, Y.; Suda, A.; Shinjoh, H. Reversible Changes in the Pt Oxidation State and Nanostructure on a Ceria-Based Supported Pt. *J Catal* **2009**, *266* (2), 182–190. DOI:10.1016/j.jcat.2009.06.005.
(43) Biesinger, M. C.; Lau, L. W. M.; Gerson, A. R.; Smart, R. St. C. Resolving Surface Chemical States in XPS Analysis of First Row Transition Metals, Oxides and Hydroxides: Sc, Ti, V, Cu and Zn. *Appl Surf Sci* **2010**, *257* (3), 887–898. DOI:10.1016/j.apsusc.2010.07.086.
(44) Landoulsi, J.; Genet, M. J.; Fleith, S.; Touré, Y.; Liascukiene, I.; Méthivier, C.; Rouxhet, P. G. Organic Adlayer on Inorganic Materials: XPS Analysis Selectivity to Cope with Adventitious Contamination. *Appl Surf Sci* **2016**, *383*, 71–83. DOI:10.1016/j.apsusc.2016.04.147.
(45) Green, C. L.; Kucernak, A. Determination of the Platinum and Ruthenium Surface Areas in Platinum−Ruthenium Alloy Electrocatalysts by Underpotential Deposition of Copper. I. Unsupported Catalysts. *Journal of Physical Chemistry B* **2002**, *106* (5), 1036–1047. DOI:10.1021/jp0131931.
(46) Krylova, G.; Na, C. Photoinduced Crystallization and Activation of Amorphous Titanium Dioxide. *The Journal of Physical Chemistry C* **2015**, *119* (22), 12400–12407. DOI:10.1021/acs.jpcc.5b02048.
(47) Wang, L.; Li, W.; Zhang, M.; Tao, K. The Interactions between the NiB Amorphous Alloy and TiO2 Support in the NiB/TiO2 Amorphous Catalysts. *Appl Catal A Gen* **2004**, *259* (2), 185–190. DOI:10.1016/j.apcata.2003.09.037.
(48) Cueva, P.; Hovden, R.; Mundy, J. A.; Xin, H. L.; Muller, D. A. Data Processing for Atomic Resolution Electron Energy Loss Spectroscopy. *Microscopy and Microanalysis* **2012**, *18* (4), 667–675. DOI:10.1017/s1431927612000244.
(49) Stoyanov, E.; Langenhorst, F.; Steinle-Neumann, G. The Effect of Valence State and Site Geometry on Ti L3,2 and O K Electron Energy-Loss Spectra of TixOy Phases. *American Mineralogist* **2007**, *92* (4), 577–586. DOI:10.2138/am.2007.2344.
(50) Landoulsi, J.; Genet, M. J.; Fleith, S.; Touré, Y.; Liascukiene, I.; Méthivier, C.; Rouxhet, P. G. Organic Adlayer on Inorganic Materials: XPS Analysis Selectivity to Cope with

Adventitious Contamination. *Appl Surf Sci* **2016**, *383*, 71–83. DOI:10.1016/j.apsusc.2016.04.147.
(51) Burke, A. R.; Brown, C. R.; Bowling, W. C.; Glaub, J. E.; Kapsch, D.; Love, C. M.; Whitaker, R. B.; Moddeman, W. E. Ignition Mechanism of the Titanium–Boron Pyrotechnic Mixture. *Surface and Interface Analysis* **1988**, *11* (6–7), 353–358. DOI:10.1002/sia.740110614.
(52) Jerkiewicz, G.; Vatankhah, G.; Lessard, J.; Soriaga, M. P.; Park, Y. S. Surface-Oxide Growth at Platinum Electrodes in Aqueous H2SO4: Reexamination of Its Mechanism through Combined Cyclic-Voltammetry, Electrochemical Quartz-Crystal Nanobalance, and Auger Electron Spectroscopy Measurements. *Electrochim Acta* **2004**, *49* (9–10), 1451–1459. DOI:10.1016/j.electacta.2003.11.008.
(53) Cohen, J. L.; Volpe, D. J.; Abruña, H. D. Electrochemical Determination of Activation Energies for Methanol Oxidation on Polycrystalline Platinum in Acidic and Alkaline Electrolytes. *Physical Chemistry Chemical Physics* **2007**, *9* (1), 49–77. DOI:10.1039/b612040g.
(54) Attard, G. A.; Brew, A.; Hunter, K.; Sharman, J.; Wright, E. Specific Adsorption of Perchlorate Anions on Pt{hkl} Single Crystal Electrodes. *Physical Chemistry Chemical Physics* **2014**, *16* (27), 13689–13698. DOI:10.1039/c4cp00564c.
(55) Kamat, G. A.; Zamora Zeledón, J. A.; Gunasooriya, G. T. K. K.; Dull, S. M.; Perryman, J. T.; Nørskov, J. K.; Stevens, M. B.; Jaramillo, T. F. Acid Anion Electrolyte Effects on Platinum for Oxygen and Hydrogen Electrocatalysis. *Commun Chem* **2022**, *5* (1), 20. DOI:10.1038/s42004-022-00635-1.
(56) Baruah, B.; Deb, P. Performance and Application of Carbon-Based Electrocatalysts in Direct Methanol Fuel Cell. *Mater Adv* **2021**, *2* (16), 5344–5364. DOI:10.1039/D1MA00503K.
(57) Solla-Gullón, J.; Vidal-Iglesias, F. J.; Herrero, E.; Feliu, J. M.; Aldaz, A. CO Monolayer Oxidation on Semi-Spherical and Preferentially Oriented (1 0 0) and (1 1 1) Platinum Nanoparticles. *Electrochem commun* **2006**, *8* (1), 189–194. DOI:10.1016/j.elecom.2005.11.008.
(58) García, G.; Koper, M. T. M. Carbon Monoxide Oxidation on Pt Single Crystal Electrodes: Understanding the Catalysis for Low Temperature Fuel Cells. *ChemPhysChem* **2011**, *12* (11), 2064–2072. DOI:10.1002/cphc.201100247.
(59) Mcpherson, I. J.; Ash, P. A.; Jones, L.; Varambhia, A.; Jacobs, R. M. J.; Vincent, K. A. Electrochemical CO Oxidation at Platinum on Carbon Studied through Analysis of Anomalous in Situ IR Spectra. **2017**. DOI:10.1021/acs.jpcc.7b02166.
(60) Ciapina, E. G.; Santos, S. F.; Gonzalez, E. R. Electrochemical CO Stripping on Nanosized Pt Surfaces in Acid Media: A Review on the Issue of Peak Multiplicity. *Journal of Electroanalytical Chemistry* **2018**, *815*, 47–60. DOI:10.1016/j.jelechem.2018.02.047.
(61) Ciapina, E. G.; Santos, S. F.; Gonzalez, E. R. The Electro-Oxidation of Carbon Monoxide and Ethanol on Supported Pt Nanoparticles: The Influence of the Support and Catalyst Microstructure. *Journal of Solid State Electrochemistry* **2013**, *17* (7), 1831–1842. DOI:10.1007/s10008-013-2120-5.
(62) Qin, Y. H.; Li, Y.; Lv, R. L.; Wang, T. L.; Wang, W. G.; Wang, C. W. Enhanced Methanol Oxidation Activity and Stability of Pt Particles Anchored on Carbon-Doped TiO2 Nanocoating Support. *J Power Sources* **2015**, *278*, 639–644. DOI:10.1016/j.jpowsour.2014.12.096.

(63) Guo, X.; Guo, D. J.; Qiu, X. P.; Chen, L. Q.; Zhu, W. T. Excellent Dispersion and Electrocatalytic Properties of Pt Nanoparticles Supported on Novel Porous Anatase TiO2 Nanorods. *J Power Sources* **2009**, *194* (1), 281–285. DOI:10.1016/j.jpowsour.2009.05.035.
(64) Chen, J. M.; Sarma, L. S.; Chen, C. H.; Cheng, M. Y.; Shih, S. C.; Wang, G. R.; Liu, D. G.; Lee, J. F.; Tang, M. T.; Hwang, B. J. Multi-Scale Dispersion in Fuel Cell Anode Catalysts: Role of TiO2 towards Achieving Nanostructured Materials. *J Power Sources* **2006**, *159* (1 SPEC. ISS.), 29–33. DOI:10.1016/j.jpowsour.2006.04.135.
(65) Dey, S.; Dhal, G. C. Property and Structure of Various Platinum Catalysts for Low-Temperature Carbon Monoxide Oxidations. *Mater Today Chem* **2020**, *16*, 100228. DOI:10.1016/j.mtchem.2019.100228.
(66) Zhang, Z.; Liu, J.; Gu, J.; Su, L.; Cheng, L. An Overview of Metal Oxide Materials as Electrocatalysts and Supports for Polymer Electrolyte Fuel Cells. *Energy Environ Sci* **2014**, *7* (8), 2535–2558. DOI:10.1039/c3ee43886d.
(67) Hepel, M.; Dela, I.; Hepel, T.; Luo, J.; Zhong, C. J. Novel Dynamic Effects in Electrocatalysis of Methanol Oxidation on Supported Nanoporous TiO2 Bimetallic Nanocatalysts. *Electrochim Acta* **2007**, *52* (18), 5529–5547. DOI:10.1016/j.electacta.2007.01.056.
(68) Loichet Torres, P. A.; El-Sayed, H. A.; Schwämmlein, J. N.; Friedrich, F.; Gasteiger, H. A. Hydrogen Gas Promoted Self-Limiting Copper Monolayer Deposition on Platinum. *J Electrochem Soc* **2021**, *168* (5), 052508. DOI:10.1149/1945-7111/abfe79.
(69) Vukmirovic, M. B.; Bliznakov, S. T.; Sasaki, K.; Wang, J. X.; Adzic, R. R. Electrodeposition of Metals in Catalyst Synthesis: The Case of Platinum Monolayer Electrocatalysts. *Electrochem Soc Interface* **2011**, *20* (2), 33. DOI:10.1149/2.F04112if.
(70) Makivić, N.; Cho, J.-Y.; Harris, K. D.; Tarascon, J.-M.; Limoges, B.; Balland, V. Evidence of Bulk Proton Insertion in Nanostructured Anatase and Amorphous TiO_2 Electrodes. *Chemistry of Materials* **2021**, *33* (9), 3436–3448. DOI:10.1021/acs.chemmater.1c00840.
(71) Kakinuma, K.; Hirayama, N.; Iiyama, A.; -, al; Joghee, P.; Pylypenko, S.; Olson, T.; Röttcher, N. C.; Ku, Y.-P.; Minichova, M.; Ehelebe, K.; Cherevko, S. Comparison of Methods to Determine Electrocatalysts' Surface Area in Gas Diffusion Electrode Setups: A Case Study on Pt/C and PtRu/C. *J. Phys. Energy* **2023**, *5*, 24007. DOI:10.1088/2515-7655/acbe1b.